

# TensorBeat: Tensor Decomposition for Monitoring Multiperson Breathing Beats with Commodity WiFi

XUYU WANG, CHAO YANG, and SHIWEN MAO, Auburn University

Breathing signal monitoring can provide important clues for health problems. Compared to existing techniques that require wearable devices and special equipment, a more desirable approach is to provide contact-free and long-term breathing rate monitoring by exploiting wireless signals. In this article, we propose TensorBeat, a system to employ channel state information (CSI) phase difference data to intelligently estimate breathing rates for multiple persons with commodity WiFi devices. The main idea is to leverage the tensor decomposition technique to handle the CSI phase difference data. The proposed TensorBeat scheme first obtains CSI phase difference data between pairs of antennas at the WiFi receiver to create CSI tensors. Then canonical polyadic (CP) decomposition is applied to obtain the desired breathing signals. A stable signal matching algorithm is developed to identify the decomposed signal pairs, and a peak detection method is applied to estimate the breathing rates for multiple persons. Our experimental study shows that TensorBeat can achieve high accuracy under different environments for multiperson breathing rate monitoring.

CCS Concepts: • **Computing methodologies** → **Machine learning approaches**; • **Applied computing** → **Health care information systems**;

Additional Key Words and Phrases: Healthcare Internet of Things (IoT), vital sign monitoring, tensor decomposition, stable roommate matching, commodity WiFi, channel state information

## ACM Reference format:

Xuyu Wang, Chao Yang, and Shiwen Mao. 2017. TensorBeat: Tensor Decomposition for Monitoring Multiperson Breathing Beats with Commodity WiFi. *ACM Trans. Intell. Syst. Technol.* 9, 1, Article 8 (September 2017), 27 pages.

<https://doi.org/10.1145/3078855>

## 1 INTRODUCTION

It is estimated that 100 million Americans suffer chronic health problems such as lung disorders, diabetes, and heart disease (Boric-Lubeke and Lubecke 2002). About three-fourths of the total U.S. healthcare cost is spent on dealing with these health conditions. To reduce such costs, there is an increasing demand for long-term health monitoring in indoor environments. By tracking vital signs such as breathing and heartbeats, a patient's physical health can be timely evaluated and meaningful clues for medical problems can be provided (Rashidi and Cook 2013). For example, monitoring breathing signals can help identify sleep disorders or anomalies, as well as decreasing sudden

This work was supported in part by the U.S. National Science Foundation under grants CNS-1702957 and DMS-1736470, and by the Wireless Engineering Research and Education Center (WEREC) at Auburn University.

Authors' address: X. Wang, C. Yang, and S. Mao, Department of Electrical and Computer Engineering, Auburn University, Auburn, AL 36849-5201; emails: {XZW0029, czy0017}@tigermail.auburn.edu, smao@ieee.org.

Permission to make digital or hard copies of part or all of this work for personal or classroom use is granted without fee provided that copies are not made or distributed for profit or commercial advantage and that copies show this notice on the first page or initial screen of a display along with the full citation. Copyrights for components of this work owned by others than ACM must be honored. Abstracting with credit is permitted. To copy otherwise, to republish, to post on servers, to redistribute to lists, or to use any component of this work in other works requires prior specific permission and/or a fee. Permissions may be requested from Publications Dept., ACM, Inc., 2 Penn Plaza, Suite 701, New York, NY 10121-0701 USA, fax +1 (212) 869-0481, or [permissions@acm.org](mailto:permissions@acm.org).

© 2017 ACM 2157-6904/2017/09-ART8 \$15.00

<https://doi.org/10.1145/3078855>

infant death syndrome (SIDS) for sleeping infants (Hunt and Hauck 2006). Traditional approaches for monitoring vital signs require patients to wear special devices, such as a capnometer (Mogue and Rantala 1988) to estimate the breathing rate or a pulse oximeter (Shariati and Zahedi 2005) on the finger to track heartbeats. Smartphones are now used to estimate the breathing rate by employing a built-in gyroscope, accelerometer (Aly and Youssef 2016), and microphone (Ren et al. 2015), and for physical activity recognition using an accelerometer (Tao et al. 2016). This requires the patient to place a smartphone near-by and wear sensors in the monitoring environment. Moreover, the readily available smartphone sensors, such as accelerometer and gyroscope, can only monitor the breathing rate for a single person. Such existing approaches could be expensive, inconvenient to use, and annoying even for a short period of time. An alternative approach is needed to provide contact-free and long-term breathing monitoring at low costs.

Several RF-based systems for vital sign tracking have recently been proposed, which employ a wireless signal to monitor breathing-induced chest movements and are mainly based on radar and WiFi techniques. For radar-based vital sign monitoring, several techniques, such as Doppler radar (Droitcour et al. 2009) and ultrawideband radar (Salmi and Molisch 2011), are used to, which require special hardware operated at high frequency and at a high cost. Moreover, the Vital-Radio system employs frequency-modulated continuous wave (FMCW) radar to track breathing and heart rates (Adib et al. 2015); it requires customized hardware using a wide bandwidth from 5.46 to 7.25GHz. For WiFi-based vital signs monitoring, mmVital (Yang et al. 2016) can exploit the received signal strength (RSS) of 60GHz millimeter wave (mmWave) signals for breathing and heart rate estimation. mmVital also operates with a larger bandwidth of about 7GHz and uses a customized hardware with a mechanical rotator. Another technique called UbiBreathe uses WiFi RSS for breathing rate estimation, which, however, requires the device be placed in the line of sight (LOS) path between the transmitter and the receiver (Abdelnasser et al. 2015).

Compared to RSS, channel state information (CSI) provides fine-grained channel information in the physical layer, which can now be read from modified device drivers for several off-the-shelf WiFi network interface cards (NICs), such as the Intel WiFi Link 5300 NIC (Halperin et al. 2010) and the Atheros AR9580 chipset (Xie et al. 2015). Moreover, CSI includes both amplitude and phase values at the subcarrier level for orthogonal frequency-division multiplexing (OFDM) channels, which is a more stable and accuracy representation of channel characteristics than RSS, including the non-line of sight (NLOS) components for small-scale fading. Liu et al. (2015) use CSI amplitude data to monitor breathing and heart signals, which requires the person to remain in the sleeping mode. However, the measured CSI phase data has not been fully exploited in prior works, largely due to the random phase fluctuation resulting from asynchronous times and frequencies of the transmitter and receiver. For multiperson breathing monitoring, because the reflected components in the received signal are from the chests of multiple persons, each varies slightly due to breathing and the variations are independent. Thus, vital sign monitoring and estimation for multiple persons still remains a challenging and open problem.

In this article, we propose to utilize CSI phase difference data between antenna pairs to monitor the breathing rates of multiple persons. First, we show that when the person is in a stationary state, such as standing, sitting, or sleeping, the CSI phase difference data is highly stable in consecutively received packets, which can be leveraged for extracting the small, periodic breathing signal hidden in the received WiFi signal. In fact, phase difference is more robust than amplitude, which usually exhibits large fluctuations because of the attenuation over the link distance, obstacles, and the multipath effect. Moreover, the phase difference data captures and preserves the periodicity of breathing, when the wireless signal is reflected from the patients' chests. To extract the weak breathing signals, and more important, to distinguish among multiple persons, we propose to employ a tensor decomposition method to handle the phase difference data (Papalexakis et al.

2016; Luo et al. 2015; Hu et al. 2014). We create the CSI tensor data by increasing the dimension of CSI data, which can be used to effectively separate different breathing signals in different clusters.

We present a system called *TensorBeat*—tensor decomposition for estimating multiperson breathing *beats*—by exploiting CSI phase difference data. TensorBeat operates as follows. First, it obtains 60 CSI phase difference data from antenna pairs 1 and 2, and 2 and 3, at the receiver. Next, a data preprocessing procedure is applied to the measured phase difference data, including data calibration and Hankelization. In the data calibration phase, the direct current (DC) component and high-frequency noises are removed. In the Hankelization phase, a two-dimensional Hankel matrix is created based on the calibrated phase difference data from every subcarrier, and the rank of the Hankel matrix is analyzed. Then, we adopt canonical polyadic (CP) decomposition for estimating multipersons breathing signs and prove its uniqueness. After CP decomposition, we obtain twice the amount of breathing signals, which, however, are randomly indexed. We thus design a stable signal matching algorithm (i.e., the stable roommate problem (Irving 1985)) to identify the decomposed signal pairs for each person. Finally, we combine the decomposed signals in each pair and employ a peak detection method to estimate the breathing rate for each person.

We implement TensorBeat with commodity 5GHz WiFi devices and verify its performance with five persons over 6 months in different indoor environments, such as a computer laboratory, a through-wall scenario, and a long corridor. The results show that the proposed TensorBeat system can achieve high accuracy and high success rates for multipersons breathing rate estimation. Moreover, we demonstrate the robustness of the proposed TensorBeat system for monitoring multiperson breathing beats under a wide range of environmental parameters.

The main contributions of this article are summarized as follows:

- (1) We theoretically and experimentally verify the feasibility of leveraging CSI phase difference for breathing monitoring. In particular, we analyze the measured phase errors in detail and demonstrate that phase difference data is stable and can be used to extract breathing signs. To the best of our knowledge, we are the first to leverage phase difference for multiperson breathing rate estimation.
- (2) We are also the first to apply tensor decomposition for RF sensing-based vital signs monitoring. We use phase difference data to create a CSI tensor for all subcarriers at the three antennas of the WiFi receiver. We then incorporate CP decomposition to obtain the desired breathing signals. A stable signal matching algorithm is developed to match the decomposed signals for each person, whereas a peak detection method is used to estimate multiperson breathing rates.
- (3) We prototype the TensorBeat system with commodity 5GHz WiFi devices and demonstrate its superior performance in different indoor environments with extensive experiments. The results show that the proposed TensorBeat system can achieve high accuracy and high success rates for multiperson breathing rate estimation.

The remainder of this article is organized as follows. The preliminaries and phase difference analysis are provided in Section 2. We review TensorBeat system design and performance analysis in Section 3 and verify its performance with extensive experiments in Section 4. We review related work in Section 5. Section 6 concludes the article.

## 2 PRELIMINARIES AND PHASE DIFFERENCE INFORMATION

### 2.1 Tensor Decomposition Preliminaries

A tensor is considered a multidimensional array (Kolda and Bader 2009). The dimensions of the tensor are called *modes*, and the order of the tensor is the number of the modes. For example,

the  $N$ -order tensor is a  $N$ -mode tensor. Moreover, it is noted that a first-order tensor is a vector, a second-order tensor is a matrix, and a third-order tensor has a cubic structure. Higher-order tensors with ( $N \geq 3$ ) have a wide range of applications, such as data mining, brain data analysis, recommendation systems, wireless communications, and computer vision, and those that are healthcare and medical related (Papalexakis et al. 2016). Higher-order tensors face various computational challenges because of the exponential increase in time and space complexity. This leads to the curse of dimensionality. Fortunately, tensor decomposition as one powerful tool is leveraged for alleviating the curse by decomposing high-order tensors into a limited number of factors. In addition, it can obtain hidden feature components, thus extracting physical insight of higher-order tensors. Two main tensor decompositions techniques are Tucker decomposition and CP decomposition (Kolda and Bader 2009). We consider CP decomposition for multiperson breathing rate estimation because it can easily obtain the unique solution (Kolda and Bader 2009). We now provide some necessary definitions and equations of tensor decomposition that can be used for our proposed algorithm.

**Definition 2.1 (Frobenius Norm of a Tensor).** The Frobenius norm of a tensor  $\chi \in \mathbb{K}^{I_1 \times I_2 \times \dots \times I_N}$  is the square root of the sum of the squares of all of its elements, which is defined by

$$\|\chi\|_F = \sqrt{\sum_{i_1=1}^{I_1} \sum_{i_2=1}^{I_2} \dots \sum_{i_N=1}^{I_N} x_{i_1, i_2, \dots, i_N}^2}, \quad (1)$$

where  $\mathbb{K}$  stands for  $\mathbb{R}$  or  $\mathbb{C}$ .

**Definition 2.2 (Kronecker Product).** The Kronecker product of matrices  $A \in \mathbb{K}^{I \times J}$  and  $B \in \mathbb{K}^{M \times N}$  is denoted as  $A \otimes B$ . The result is an  $(IM) \times (JN)$  matrix, which is defined as

$$A \otimes B = \begin{bmatrix} a_{11}B & a_{12}B & \dots & a_{1J}B \\ a_{21}B & a_{22}B & \dots & a_{2J}B \\ \vdots & \vdots & \ddots & \vdots \\ a_{I1}B & a_{I2}B & \dots & a_{IJ}B \end{bmatrix}. \quad (2)$$

**Definition 2.3 (Khatri-Rao Product).** The Khatri-Rao product of  $A \in \mathbb{K}^{I \times J}$  and  $B \in \mathbb{K}^{M \times J}$  is denoted as  $A \odot B$ . It is the columnwise Kronecker product with size  $(IM) \times J$ , which is defined as

$$A \odot B = [a_1 \otimes b_1, a_2 \otimes b_2, \dots, a_J \otimes b_J]. \quad (3)$$

**Definition 2.4 (Hadamard Product).** The Hadamard product of  $A \in \mathbb{K}^{I \times J}$  and  $B \in \mathbb{K}^{I \times J}$  is denoted as  $A * B$ . It is the elementwise matrix product with size  $I \times J$ , which is defined as

$$A * B = \begin{bmatrix} a_{11}b_{11} & a_{12}b_{12} & \dots & a_{1J}b_{1J} \\ a_{21}b_{21} & a_{22}b_{22} & \dots & a_{2J}b_{2J} \\ \vdots & \vdots & \ddots & \vdots \\ a_{I1}b_{I1} & a_{I2}b_{I2} & \dots & a_{IJ}b_{IJ} \end{bmatrix}. \quad (4)$$

## 2.2 CSI Preliminaries

OFDM is an effective wireless transmission technique widely used in many wireless systems, including WiFi (e.g., IEEE 802.11 a/g/n) and LTE (Wang et al. 2016c; Xu et al. 2014). The OFDM system partitions the wireless channel into multiple orthogonal subcarriers, where data is transmitted over all subcarriers by using the same modulation and coding scheme (MCS) to combat frequency selective fading. With a modified device driver for off-the-shelf NICs, such as the Intel 5300 NIC (Halperin et al. 2010) and the Atheros AR9580 chipset (Xie et al. 2015), the CSI data can be

extracted, which represents fine-grained physical (PHY) information. Moreover, CSI captures rich wireless channel characteristics such as shadowing fading, distortion, and the multipath effect.

The WiFi OFDM channel can be regarded as a narrowband flat fading channel, which can be expressed in the frequency domain as

$$\vec{Y} = \mathbf{H} \cdot \vec{X} + \vec{N}, \quad (5)$$

where  $\vec{Y}$  and  $\vec{X}$  denote the received and transmitted signal vectors, respectively;  $\vec{N}$  is the additive white Gaussian noise; and  $\mathbf{H}$  represents the channel frequency response, which can be estimated from  $\vec{Y}$  and  $\vec{X}$ .

Although the WiFi OFDM system can use 56 subcarriers for data transmission on a 20MHz channel, the Intel 5300 NIC device driver can only provide CSI for 30 out of the 56 subcarriers. The channel frequency response of subcarrier  $i$ , denoted by  $H_i$ , is a complex value, given as

$$H_i = \mathcal{I}_i + j\mathcal{Q}_i = |H_i| \exp(j\angle H_i), \quad (6)$$

where  $\mathcal{I}_i$  and  $\mathcal{Q}_i$  are the in-phase component and quadrature component, respectively, and  $|H_i|$  and  $\angle H_i$  are the amplitude and phase response of subcarrier  $i$ , respectively.

For indoor environments with multipath components, the channel frequency response of subcarrier  $i$ ,  $H_i$ , can also be written as

$$H_i = \sum_{k=0}^K r_k \cdot e^{-j2\pi f_i \tau_k}, \quad (7)$$

where  $K$  is the number of multipath components, and  $r_k$  and  $\tau_k$  are the attenuation and propagation delay on the  $k$ th path, respectively.

Traditionally, the multipath components are regarded as harmful for wireless communications, as they cause the delay spread (requires guard times) and large fluctuation of received wireless signal (harder to demodulate). For indoor localization systems, multiple signals will be received from a single transmission, including one LOS signal and many reflected signals. It is a challenging problem to detect the LOS signal from the mixed multipath components, which is indicative of the direction of the transmitter (Yang et al. 2013; Wang et al. 2014b). In this article, however, we take a different view and show that the multiple signals reflected from the chests of multiple persons can be useful for estimating their breathing rates simultaneously.

### 2.3 Phase Difference Information

As discussed, we exploit phase difference information for breathing rate estimation. We verify that the phase difference values between two adjacent antennas are stable for consecutively received packets in this section. In fact, the extracted phase information from the Intel 5300 NIC is highly random and cannot be used for breathing monitoring. This is because of the asynchronous times and frequencies of transmitter and receiver NICs. Two effective techniques have been proposed for CSI phase calibration to remove the unknown random components in CSI phase data. The first technique is to take a linear transformation for the CSI phase data over all subcarriers (Qian et al. 2014; Wang et al. 2015b, 2016b). The other technique is to use the phase difference between two adjacent antennas (in the 2.4GHz band) and to remove the measured average of phase difference for LOS recognition (Wu et al. 2015). It can be seen that these techniques only obtain the stable phase information and phase difference data with a zero mean, respectively, but none of these are useful for breathing rate estimation.

To prove the stability of measured CSI phase difference in the 5GHz band, we write the measured phase of subcarrier  $i$ , denoted as  $\angle\hat{H}_i$ , per Speth et al. (1999):

$$\angle\hat{H}_i = \angle H_i + (\lambda_p + \lambda_s)m_i + \lambda_c + \beta + Z, \quad (8)$$

where  $\angle H_i$  is the true phase of CSI data,  $m_i$  is the subcarrier index of subcarrier  $i$ ,  $\beta$  is the initial phase offset at the phase-locked loop (PLL),  $Z$  is the measurement environment noise, and  $\lambda_p$ ,  $\lambda_s$ , and  $\lambda_c$  are the phase errors from packet boundary detection (PBD), the sampling frequency offset (SFO), and the central frequency offset (CFO), respectively (Speth et al. 1999), which are given by

$$\begin{cases} \lambda_p = 2\pi \frac{\Delta t}{N} \\ \lambda_s = 2\pi \left( \frac{T'-T}{T} \right) \frac{T_s}{T_u} n \\ \lambda_c = 2\pi \Delta f T_s n, \end{cases} \quad (9)$$

where  $\Delta t$  is the PBD delay;  $N$  is the FFT size;  $T'$  and  $T$  are the sampling periods from the receiver and the transmitter, respectively;  $T_u$  is the length of the data symbol;  $T_s$  is the total length of the data symbol and the guard interval;  $n$  is the sampling time offset for the current packet; and  $\Delta f$  is the center frequency difference between the transmitter and receiver. In fact, the values of  $\Delta t$ ,  $\frac{T'-T}{T}$ ,  $n$ ,  $\Delta f$ , and  $\beta$  in (8) and (9) are unknown, and the values of  $\lambda_p$ ,  $\lambda_s$ , and  $\lambda_c$  can be different for different packets. Thus, we cannot obtain the true phase  $\angle H_i$  from measured phase values.

However, the measured phase difference on subcarrier  $i$  is stable, which can be employed for breathing rate estimation. Since the three antennas of the Intel 5300 NIC are on the same NIC, they use the same system clock and the same down-converter frequency. The measured CSI phases on subcarrier  $i$  from two adjacent antennas have the same  $\lambda_p$ ,  $\lambda_s$ ,  $\lambda_c$ , and  $m_i$ . The phase difference can be computed as

$$\Delta\angle\hat{H}_i = \Delta\angle H_i + \Delta\beta + \Delta Z, \quad (10)$$

where  $\Delta\angle H_i$  is the true phase difference of subcarrier  $i$ ;  $\Delta\beta$  is the unknown difference in phase offsets, which is a constant (Gjengset et al. 2014); and  $\Delta Z$  is the noise difference. Since in (10) the random values  $\Delta t$ ,  $\Delta f$ , and  $n$  are all removed, the phase difference becomes more stable for back-to-back received packets. As an example, we plot in Figure 1 the phase differences (marked as red dots) and the single antenna phases (marked as gray crosses) read from the third subcarrier for 500 consecutively received packets. It can be seen that the single antenna phase is nearly uniformly distributed between 0 and 360 degrees. However, all phase difference data concentrate in a small sector between 330 and 340 degrees, which is significantly more stable than phase data.

Breathing rate estimation for multiple persons is a challenging problem because the reflected components in the received signal are from the chests of multiple persons, each moves slightly due to breathing, and the movements are independent. Thus, the peak-to-peak detection method cannot be effective for detecting the multiple breathing signals from the received signal. The aggregated breathing signal from multiple persons is not a clearly periodic signal anymore. Figure 2 shows the detected breathing signals for one person (the upper plot) and three persons (the lower plot). We can see that for one person, the breathing signal exhibits a noticeable periodicity. Thus, the breathing rate can be estimated by peak detection after removing the noise. However, the aggregated breathing signal of three persons does not show noticeable periodicity for packets 400 to 600. Traditional FFT-based methods can transform the received signal from the time domain to the frequency domain to estimate the breathing frequencies from multiple persons. Figure 3 shows the breathing rate estimation for one person (the upper plot) and three persons (the lower plot) with the FFT method. We can see that the estimated frequency for one person is 0.2Hz, which is almost the same as the true breathing rate. However, for three-person breathing rate estimation, the FFT curve only has two peaks, and the estimated breathing rates are much less accurate. In particular,



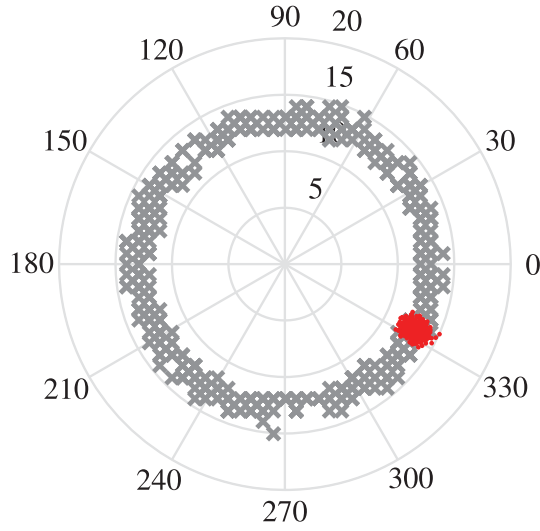


Fig. 1. Phase differences (marked by red dots) and single antenna phases (marked by gray crosses) of the third subcarrier for 500 back-to-back packets, plotted in the polar coordinate system.

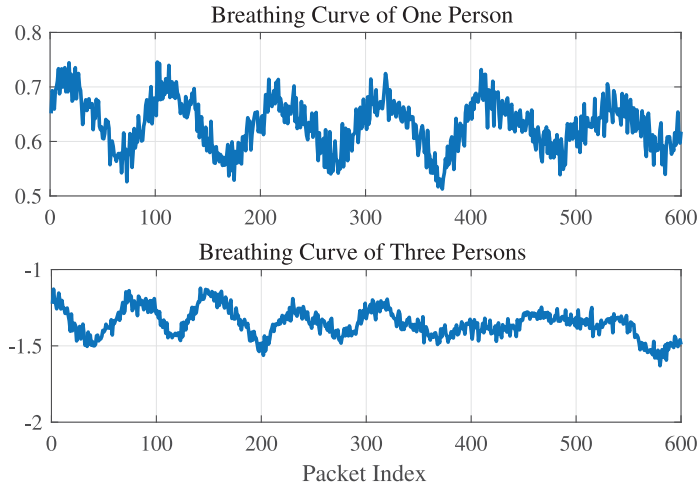


Fig. 2. Detected breathing signals for one person (the upper plot) and three persons (the lower plot).

the third peak cannot be estimated. This is because FFT-based methods require a larger window size to improve the frequency resolution. We show that the proposed tensor decomposition-based method is highly effective for multiperson breathing rate estimation in the following section.

### 3 THE TENSORBEAT SYSTEM

#### 3.1 TensorBeat System Architecture

The main idea of the proposed TensorBeat system is to estimate multiperson breathing rates by employing a tensor decomposition method. To obtain CSI tensor data, we first create a two-dimensional Hankel matrix with phase difference data from back-to-back received packets extracted from each subcarrier at each antenna. Then, by leveraging the phase differences from

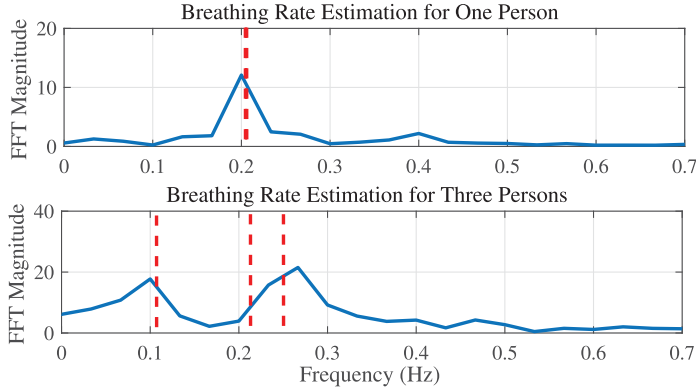


Fig. 3. Breathing rate estimation for one person (the upper plot) and three persons (the lower plot) based on FFT.

the 60 subcarriers (i.e., that between antennas 1 and 2, and between antennas 2 and 3), we can construct the third dimension of the CSI tensor data. The TensorBeat system will then leverage the created CSI tensor to estimate multiperson breathing signals. Our approach is motivated by two observations. First, for stationary modes of a person, such as standing, sitting, or sleeping, CSI phase difference from consecutively received packets is highly stable. It can thus be useful for extracting the periodic breathing signals. Second, the tensor decomposition method can effectively estimate multiperson breathing beats. We create the CSI tensor data by increasing the dimension of CSI data from one to three. The higher-dimension CSI data is helpful to effectively separate different breathing signals by forming different clusters. This strategy is similar to the kernel method in traditional machine learning, such as support vector machine (SVM) (Wu et al. 2007) or multiple hidden layers in deep learning (LeCun et al. 2015; Wang et al. 2015b, 2015c, 2017a, 2017b).

As shown in Figure 4, the TensorBeat system consists of five main modules: Data Extraction, Data Preprocessing, CP Decomposition, Signal Matching, and Breathing Rate Estimation. For Data Extraction, TensorBeat obtains 60 CSI phase difference data, 30 between antennas 1 and 2, and 30 between antennas 2 and 3, at the receiver with an off-the-shelf WiFi device. The Data Preprocessing module includes data calibration and Hankelization. Data calibration is implemented to remove the DC component and high-frequency noises. Hankelization creates a two-dimensional Hankel matrix with phase difference data from each subcarrier for back-to-back received packets. The rank of the constructed Hankel matrix is then analyzed. We next apply CP Decomposition to estimate multiperson breathing signals and prove its uniqueness. For Signal Matching, we first compute the autocorrelation function of the decomposed signals and incorporate a stable roommate matching algorithm to identify the decomposed signal pairs for each person, where a preference list is computed with the dynamic time warping (DTW) values of the autocorrelation signals. For Breathing Rate Estimation, we combine the decomposed signals in each pair and use the peak detection method to compute the breathing rate for each person.

The Data Extraction module has a similar design as our prior work PhaseBeat (Wang et al. 2017b). In the remainder of this section, we present the design and analysis of the remaining four modules of the TensorBeat system in detail.

### 3.2 Data Preprocessing

**3.2.1 Data Calibration.** We use a 20Hz sampling rate to obtain 60 CSI phase difference data, 30 between antennas 1 and 2, and 30 between antennas 2 and 3, at the receiver with an off-the-shelf



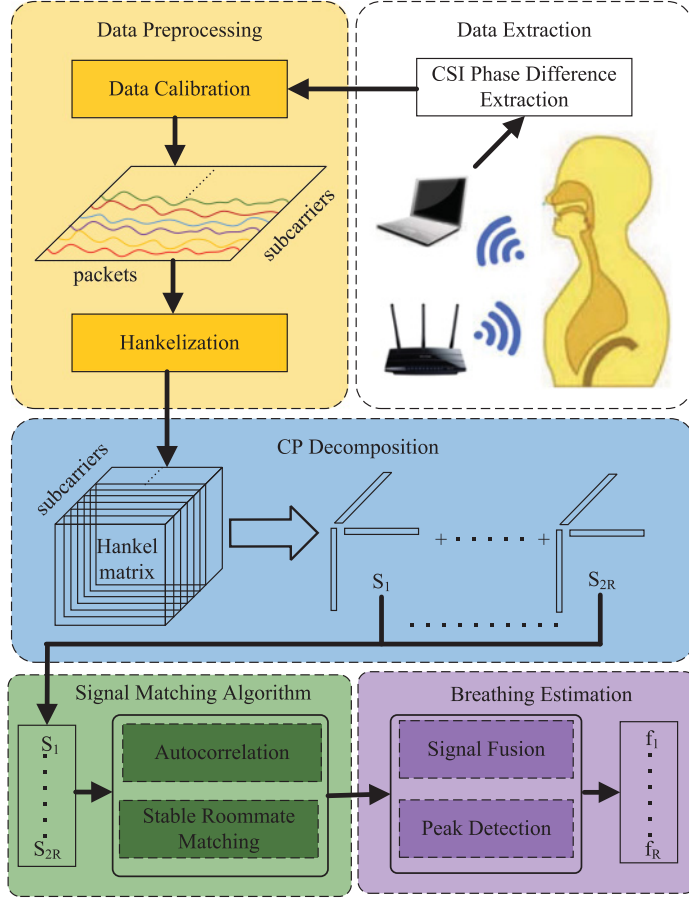


Fig. 4. TensorBeat system architecture.

WiFi device at 5GHz for data extraction. Then, data calibration is applied to remove the DC component and high-frequency noises. Because the DC component is also considered a kind of signal, which may affect CSI tensor decomposition, TensorBeat adopts the Hampel filter to remove the DC component. Unlike traditional data calibration approaches that only remove the high-frequency noise, we use the Hampel filter for detrending the original CSI phase difference data. In fact, the Hampel filter, which is set as a large sliding window with 150 samples wide and a small threshold of 0.001, is first used to extract the basic trend of the original data. Then, the detrended data is generated by subtracting the basic trend data from the original data. We also utilize the Hampel filter to reduce the high-frequency noise by using a sliding window of 6 samples wide and a threshold of 0.01.

Figure 5 presents an example of data calibration. We can see that the original phase differences of all subcarriers have both a DC component and high-frequency noises. With the proposed data calibration approach, the DC components are readily removed and all subcarriers demonstrate a similar calibrated signal over the 600 packet range with low noise. Such calibrated signal will then be used for estimating the breathing rates of multiple persons.

**3.2.2 Hankelization.** After data calibration, we obtain the CSI phase difference data matrix with a dimension of (number of packets  $\times$  number of subcarriers). We then employ a Hankelization

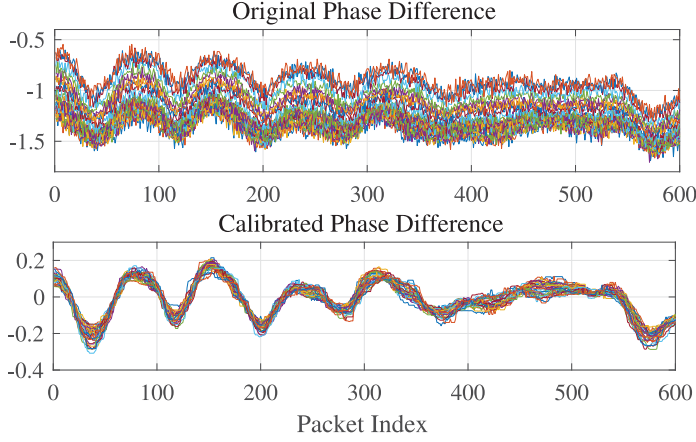


Fig. 5. Data calibration: an example.

method to transform the large CSI matrix into a CSI tensor by expanding the packets into an additional dimension (Lathauwer 2011). Specifically, we rearrange the signals of each subcarrier into a two-dimensional Hankel matrix so that the signals from all 60 subcarriers can be considered as a three-dimensional tensor. Define  $H_r$  as the constructed Hankel matrix with the size  $I \times J$  for subcarrier  $r$ , which is created by mapping  $N$  packets onto the Hankel matrix with  $N = I + J - 1$ . We consider the Hankel matrix with size  $I = J = \frac{N+1}{2}$ . We thus obtain the Hankel matrix  $H_r$  for subcarrier  $r$  as

$$\mathbf{H}_r = \begin{bmatrix} h_r(0) & h_r(1) & \dots & h_r(\frac{N+1}{2} - 1) \\ h_r(1) & h_r(2) & \dots & h_r(\frac{N+1}{2}) \\ \vdots & \vdots & \ddots & \vdots \\ h_r(\frac{N+1}{2} - 1) & h_r(\frac{N+1}{2}) & \dots & h_r(N - 1) \end{bmatrix}, \quad (11)$$

where  $h_r(i)$  is the calibrated phase difference data from subcarrier  $r$  for packet  $i$ . In our experiments, we set  $N = 599$  and  $I = J = 300$ . To determine the number of components needed for CSI tensor decomposition, we provide the following theorem for estimating  $R$  breathing signals.

**THEOREM 3.1.** *If there are  $R$  breathing signals in an indoor monitoring environment, the constructed Hankel matrix  $\mathbf{H}_r$  for subcarrier  $r$  has a rank of  $2R$  when noise is negligible.*

**PROOF.** When analyzing signal data structure, we assume that noise is negligible. Moreover, let the  $i$ th breathing signal be represented as  $S_i(t) = A_i \cos(w_i t + \varphi_i)$ . The observed signal from a subcarrier can be represented by Cichocki et al. (2015):

$$Y(t) = \sum_{i=1}^R K_i S_i(t) = \sum_{i=1}^R \hat{K}_i \cos(w_i t + \varphi_i), \quad (12)$$

where  $K_i$  is the coefficient for breathing signal  $i$  and the new coefficient  $\hat{K}_i = K_i A_i$ . The  $i$ th component of  $Y(t)$ ,  $\hat{K}_i \cos(w_i t + \varphi_i)$ , can be decomposed using Euler's formula. We have

$$\begin{aligned} \hat{K}_i \cos(w_i t + \varphi_i) &= \frac{\hat{K}_i}{2} \exp(j(w_i t + \varphi_i)) + \frac{\hat{K}_i}{2} \exp(j(-w_i t - \varphi_i)) \\ &= \frac{\hat{K}_i}{2} \exp(j\varphi_i) \exp(jw_i t) + \frac{\hat{K}_i}{2} \exp(-j\varphi_i) \exp(-jw_i t). \end{aligned} \quad (13)$$

Each breathing signal can be separated into two exponential signals with different coefficients. Combining all the  $R$  breathing signals, we have

$$\begin{aligned} Y(t) &= \sum_{i=1}^R \left( \frac{\hat{K}_i}{2} \exp(j\varphi_i) \exp(jw_i t) + \frac{\hat{K}_i}{2} \exp(-j\varphi_i) \exp(-jw_i t) \right) \\ &= \sum_{i=1}^{2R} \tilde{K}_i Z_i^t, \end{aligned} \quad (14)$$

where the updated signal  $Z_i^t$  is denoted as  $Z_i^t = \exp(\pm jw_i t)$  and  $\tilde{K}_i = \frac{\hat{K}_i}{2} \exp(\pm j\varphi_i)$  is its coefficient. For packets received at discrete times, we represent the received signal as  $Y(n) = \sum_{i=1}^{2R} \tilde{K}_i Z_i^n$ . Note that the combined signal can be considered as an exponential polynomial with  $2R$  different exponential terms. Mapping signal  $Y(n)$  for  $n = 1, 2, \dots, N$  into a Hankel matrix with size  $I = J = \frac{N+1}{2}$ , we have

$$H_r = \begin{bmatrix} \sum_{i=1}^{2R} \tilde{K}_i Z_i^0 & \sum_{i=1}^{2R} \tilde{K}_i Z_i^1 & \cdots & \sum_{i=1}^{2R} \tilde{K}_i Z_i^{\frac{N+1}{2}-1} \\ \sum_{i=1}^{2R} \tilde{K}_i Z_i^1 & \sum_{i=1}^{2R} \tilde{K}_i Z_i^2 & \cdots & \sum_{i=1}^{2R} \tilde{K}_i Z_i^{\frac{N+1}{2}} \\ \vdots & \vdots & \cdots & \vdots \\ \sum_{i=1}^{2R} \tilde{K}_i Z_i^{\frac{N+1}{2}-1} & \sum_{i=1}^{2R} \tilde{K}_i Z_i^{\frac{N+1}{2}} & \cdots & \sum_{i=1}^{2R} \tilde{K}_i Z_i^{N-1} \end{bmatrix}. \quad (15)$$

We can see that the Hankel matrix can be decomposed with Vandermonde decomposition (Lathauwer 2011) as

$$H_r = V_r \cdot \text{diag}(\tilde{K}_1, \tilde{K}_1, \dots, \tilde{K}_{2R}) \cdot \tilde{V}_r^T, \quad (16)$$

where the Vandermonde matrices  $V_r \in \mathbb{K}^{\frac{N+1}{2} \times 2R}$  and  $\tilde{V}_r \in \mathbb{K}^{\frac{N+1}{2} \times 2R}$  are given by

$$V_r = \tilde{V}_r = \begin{bmatrix} 1 & 1 & \cdots & 1 \\ Z_1 & Z_2 & \cdots & Z_{2R} \\ \vdots & \vdots & \cdots & \vdots \\ Z_1^{\frac{N+1}{2}-1} & Z_2^{\frac{N+1}{2}-1} & \cdots & Z_{2R}^{\frac{N+1}{2}-1} \end{bmatrix}. \quad (17)$$

Because a Vandermonde matrix is full rank, which is obtained by different poles, the rank of the Hankel matrix generated by  $R$  breathing signals is  $2R$ .  $\square$

According to Theorem 3.1,  $2R$  signal components are required to separate the  $R$  breathing signals. Next, we consider the influence of measurement noise on the Hankel matrix  $H_r$ . Because of noise, the Hankel matrix  $H_r$  is actually a full-rank matrix. However, Theorem 3.1 shows that the rank of the combined breathing signal is  $2R$ , meaning that the first  $2R$  weighted decomposed components are much stronger than the remaining ones as long as the signal-to-noise ratio (SNR) is not very low. This shows that the Hankel matrix structure can be used to effectively separate breathing signals from white noise. Actually, the different signals will be well denoised and separated by using tensor decomposition, which is discussed in Section 3.3.

### 3.3 CP Decomposition

Once the CSI tensor is ready, we apply CP decomposition to estimate multiperson breathing signals. With CP decomposition, the CSI tensor data can be approximated as the sum of  $2R$  rank-one tensors according to Theorem 3.1. Denote  $\chi \in \mathbb{K}^{I \times J \times K}$  as a third-order CSI tensor, which can be

obtained by the sum of three-way outer products as in Kolda and Bader (2009) and Papalexakis et al. (2016):

$$\chi \approx \sum_{r=1}^{2R} a_r \circ b_r \circ c_r, \quad (18)$$

where  $a_r$ ,  $b_r$ , and  $c_r$  are the vectors at the  $r$ th position for the first, second, and third dimension, respectively, and  $2R$  is the number of decomposition components, which is the approximation rank of the tensor based on CP decomposition (Sun and Kumar 2014, 2015). Their outer product is defined by

$$(a_r \circ b_r \circ c_r)(i, j, k) = a_r(i)b_r(j)c_r(k), \quad \text{for all } i, j, k. \quad (19)$$

We consider factor matrices  $\mathbf{A} = [a_1, a_2, \dots, a_{2R}] \in \mathbb{K}^{I \times 2R}$ ,  $\mathbf{B} = [b_1, b_2, \dots, b_{2R}] \in \mathbb{K}^{J \times 2R}$ , and  $\mathbf{C} = [c_1, c_2, \dots, c_{2R}] \in \mathbb{K}^{K \times 2R}$  as the combination of vectors from rank-one components. Moreover, define  $\mathcal{X}_{(1)} \in \mathbb{K}^{I \times JK}$ ,  $\mathcal{X}_{(2)} \in \mathbb{K}^{J \times IK}$ , and  $\mathcal{X}_{(3)} \in \mathbb{K}^{K \times IJ}$  as 1-mode, 2-mode, and 3-mode matricization of CSI tensor  $\chi \in \mathbb{K}^{I \times J \times K}$ , respectively, which are obtained by fixing one mode and arranging the slices of the rest of the modes into a long matrix (Kolda and Bader 2009). Then, we can write the three matricized forms as

$$\mathcal{X}_{(1)} \approx \mathbf{A}(\mathbf{C} \odot \mathbf{B})^T, \quad (20)$$

$$\mathcal{X}_{(2)} \approx \mathbf{B}(\mathbf{C} \odot \mathbf{A})^T, \quad (21)$$

$$\mathcal{X}_{(3)} \approx \mathbf{C}(\mathbf{B} \odot \mathbf{A})^T, \quad (22)$$

where  $\odot$  denotes the Khatri-Rao product.

When the number of components  $2R$  is given, we apply the alternating least squares (ALS) algorithm, the most widely used algorithm for CP decomposition (Kolda and Bader 2009). To decompose the CSI tensor, we minimize the square sum of the differences between the CSI tensor  $\chi$  and the estimated tensor:

$$\min_{\mathbf{A}, \mathbf{B}, \mathbf{C}} \left\| \chi - \sum_{r=1}^{2R} a_r \circ b_r \circ c_r \right\|_F^2. \quad (23)$$

Note that (23) is not convex. However, the ALS algorithm can effectively solve the problem by fixing two of the factor matrices to reduce the problem to a linear least squares problem with the third factor matrix as variable. If we fix  $\mathbf{B}$  and  $\mathbf{C}$ , we can rewrite problem (23) as

$$\min_{\mathbf{A}} \left\| \mathcal{X}_{(1)} - \mathbf{A}(\mathbf{C} \odot \mathbf{B})^T \right\|_F^2. \quad (24)$$

We can derive the optimal solution to problem (24) as  $\mathbf{A} = \mathcal{X}_{(1)}[(\mathbf{C} \odot \mathbf{B})^T]^\dagger$ . Applying the property of pseudoinverse of the Khatri-Rao product, it follows that

$$\mathbf{A} = \mathcal{X}_{(1)}(\mathbf{C} \odot \mathbf{B})(\mathbf{C}^T \mathbf{C} * \mathbf{B}^T \mathbf{B})^\dagger, \quad (25)$$

where  $*$  denotes the Hadamard product. This equation only requires computing the pseudoinverse of a  $2R \times 2R$  matrix rather than a  $JK \times 2R$  matrix. Note that  $R$  is much smaller than  $J$  and  $K$ , and thus the computing complexity can be greatly reduced. Similarly, we can obtain the optimal solutions for  $\mathbf{B}$  and  $\mathbf{C}$  as

$$\mathbf{B} = \mathcal{X}_{(2)}(\mathbf{C} \odot \mathbf{A})(\mathbf{C}^T \mathbf{C} * \mathbf{A}^T \mathbf{A})^\dagger, \quad (26)$$

$$\mathbf{C} = \mathcal{X}_{(3)}(\mathbf{B} \odot \mathbf{A})(\mathbf{B}^T \mathbf{B} * \mathbf{A}^T \mathbf{A})^\dagger. \quad (27)$$

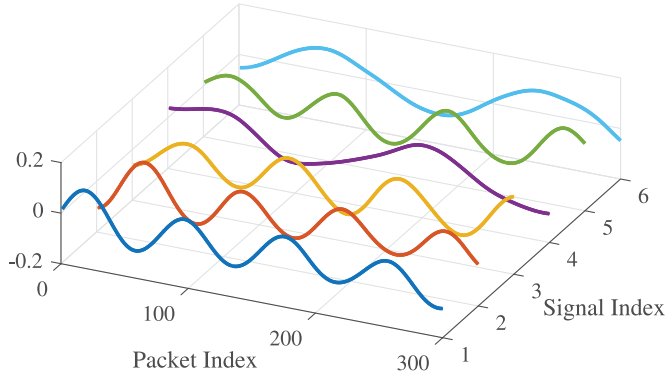


Fig. 6. CP decomposition results for a CSI tensor of three persons.

Applying ALS to CP decomposition, we obtain matrices  $\mathbf{A}$ ,  $\mathbf{B}$ , and  $\mathbf{C}$ . To guarantee the effectiveness of the decomposed components, we next examine the uniqueness of CP decomposition. The basic theorem on the uniqueness of CP decomposition is given in Kolda and Bader (2009), which is provided in the following.

**FACT 1.** *For tensor  $\chi$  with rank  $L$ , if  $k_A + k_B + k_C \geq 2L + 2$ , then the CP decomposition of  $\chi$  is unique, where  $k_A$ ,  $k_B$ , and  $k_C$  denote the  $k$ -rank of matrices  $\mathbf{A}$ ,  $\mathbf{B}$ , and  $\mathbf{C}$ , respectively. Here  $k$ -rank means the maximum value  $k$  such that any  $k$  columns are linearly independent (Kolda and Bader 2009).*

Based on Fact 1, we have the following theorem for the CP decomposition.

**THEOREM 3.2.** *For the proposed CSI tensor  $\chi$  with rank  $2R$ , the CP decomposition of  $\chi$  is unique.*

**PROOF.** The proposed CSI tensor  $\chi$  is created by  $K$  Hankel matrix, where the  $r$ th Hankel matrix  $H_r$  is rank- $2R$  according to Theorem 3.1. Thus, for the  $k$ -rank of matrices  $\mathbf{A}$  and  $\mathbf{B}$ , we have  $k_A = 2R$  and  $k_B = 2R$ . However, because phase differences of subcarriers between antennas 1 and 2 and antennas 2 and 3 are independent, the  $k$ -rank of matrix  $\mathbf{C}$  is  $k_C \geq 2$ . Thus, we have  $k_A + k_B + k_C \geq 2R + 2R + 2 = 2(2R) + 2$ , which satisfies the conditions in Fact 1. This proves the theorem.  $\square$

Theorem 3.2 indicates that the CP decomposition of the created CSI tensor is unique, which can be used to effectively estimate multiple breathing rates. In the proposed TensorBeat system, we leverage matrix  $\mathbf{A} = [a_1, a_2, \dots, a_{2R}]$  as decomposed signals  $S_1, S_2, \dots, S_{2R}$ . For example, Figure 6 shows the results of CP decomposition for CSI tensor data from three persons ( $R = 3$ ). We can see that there are six signals. Moreover, signals 1 and 2 are similar, signals 3 and 5 are similar, and signals 4 and 6 are similar. This is because CP decomposition cannot guarantee that similar signals are located at adjacent locations (i.e., the output signals are randomly indexed). Thus, we need to identify the signal pairs among the decomposed signals for each person, which will be addressed in Section 3.4.

### 3.4 Signal Matching Algorithm

The CP decomposition of CSI tensor data yields  $2R$  decomposed signals (i.e.,  $S_1, S_2, \dots, S_{2R}$ ), which, however, are randomly indexed. In this section, we propose a signal matching algorithm to pair the two similar decomposed signals that belong to the same person. The main idea is to leverage autocorrelation to strengthen the periodicity of decomposed signals and use the DTW method

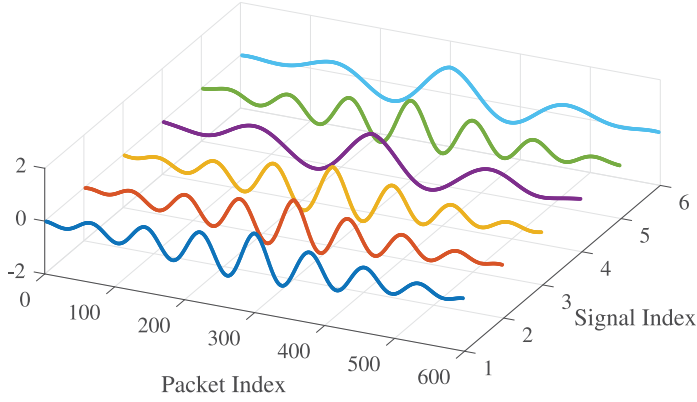


Fig. 7. Autocorrelation of the decomposed breathing signals.

to compute the similarity value for any pair of signals. Finally, we apply the stable roommate matching algorithm to pair the decomposed signals for each person using the DTW values as the closeness metric. We introduce the proposed signal matching algorithm in the following.

**3.4.1 Autocorrelation and DTW.** After CP decomposition, we first compute the autocorrelation function of the 2R decomposed signals to strengthen their periodicity. We evaluate the autocorrelation function of the decomposed signals for two reasons. The first is that the autocorrelation of a decomposed signal can increase the data length, which helps to improve the accuracy of the peak detection. Second, because the decomposed signals have phase shift and nonalignment, using the autocorrelation of decomposed signals can reduce such shifts and strengthen the periodicity of the decomposed signals. Figure 7 shows the autocorrelation of the decomposed breathing signals produced by CP decomposition. We can see that each autocorrelation signal exhibits a more obvious periodicity than that of the original decomposition signals. Moreover, the data length is increased from 300 to 600.

Furthermore, we employ the DTW approach to measure the distance between any pair of autocorrelation signals, which is different from the Euclidean distance method that computes the sum of distances from each value on one curve to the corresponding value on the other curve. Moreover, the Euclidean distance method believes that two autocorrelation signals with the same length are different as long as one of them has a small shift. However, DTW can automatically identify these shifts and provide the similar distance measurement between two autocorrelation signals by aligning the corresponding time series, thus overcoming the limitation of the Euclidean distance method.

With the autocorrelation signals, we design the DTW method for measuring their pairwise distance. Given two autocorrelation signals and a cost function, the DTW method seeks an alignment by matching each point in the first autocorrelation signal to one or more points in the second signal, thus minimizing the cost function for all points (Wang and Katabi 2013; Salvador and Chan 2004, 2007). To reduce the computational complexity of DTW, we apply downsampling to the two autocorrelation signals, which leads to a reduced number of packets  $N'$ . Then, considering two downsampled autocorrelation signals  $P_i = [P_i(0), P_i(1), \dots, P_i(N' - 1)]$  and  $P_j = [P_j(0), P_j(1), \dots, P_j(N' - 1)]$ , we need to find a warping path  $W = [w_1, w_2, \dots, w_L]$ , where  $L$  is the length of the path and the  $l$ th element of the warping path is  $w_l = (m_l, n_l)$ , where  $m$  and  $n$  are the packet index for the two downsampled autocorrelation signals. The objective is to minimize the total cost function by implementing the nonlinear mapping between two



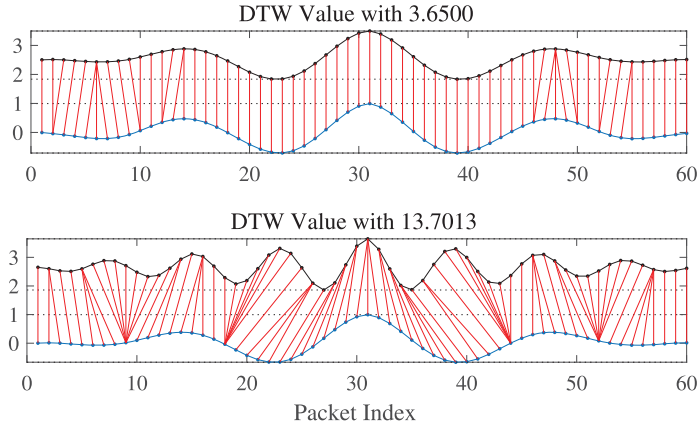


Fig. 8. DTW results for downsampled autocorrelation signals 4 and 6 (the upper plot) and downsampled autocorrelation signals 4 and 3 (the lower plot), respectively.

downsampled autocorrelation signals  $P_i$  and  $P_j$ . The formulated problem is given by

$$\min \sum_{l=1}^L \|P_i(m_l) - P_j(n_l)\| \quad (28)$$

$$\text{subject to } (m_1, n_1) = (0, 0) \quad (29)$$

$$(m_L, n_L) = (N' - 1, N' - 1) \quad (30)$$

$$m_l \leq m_{l+1} \leq m_l + 1 \quad (31)$$

$$n_l \leq n_{l+1} \leq n_l + 1. \quad (32)$$

The objection function is to minimize the distance between two downsampled autocorrelation signals. The first and second constraints are boundary constraints, which require that the warping path starts at  $P_i(0)$  and  $P_j(0)$  and ends at  $P_i(N' - 1)$  and  $P_j(N' - 1)$ . This can guarantee that all points of the two downsampled autocorrelation signals are used for measuring their distance, thus avoiding to use only local data. Furthermore, the third and fourth constraints are monotonic and marching constraints, which require that there are no cycles for  $w_i$  and  $w_j$  in the warping path and the path is increased with the maximum 1 at each step.

We apply dynamic programming to solve problem (28) to obtain the minimum distance warping path between two downsampled autocorrelation signals. We consider a two-dimensional cost matrix  $C$  with size  $N' \times N'$ , whose element  $C(m_l, n_l)$  is the minimum distance warping path for two downsampled autocorrelation signals  $P_i = [P_i(0), P_i(1), \dots, P_i(m_l)]$  and  $P_j = [P_j(0), P_j(1), \dots, P_j(n_l)]$ . We design the recurrence equation in dynamic programming as follows:

$$C(m_l, n_l) = \|P_i(m_l) - P_j(n_l)\| + \min [C(m_l - 1, n_l), C(m_l, n_l - 1), C(m_l - 1, n_l - 1)]. \quad (33)$$

By filling all elements of the cost matrix  $C$ , the value  $C(N' - 1, N' - 1)$  can be computed as the DTW value between the two downsampled autocorrelation signals. The time complexity is  $O(N'^2)$ . Figure 8 shows the DTW results for downsampled autocorrelation signals 4 and 6 (the upper plot) and downsampled autocorrelation signals 4 and 3 (the lower plot), where we set the downsampling number of packets as  $N' = \frac{N}{10} = 60$ . It can be seen that downsampled autocorrelation signals 4 and

6 have a smaller DTW value (i.e., 3.65) than downsampled autocorrelation signals 4 and 3 (i.e., 13.7). In other words, signals 4 and 6 are more similar and more likely to belong to the same person. We also find that the downsampled autocorrelation signals have a high similarity in the center than that on the boundary, and it can reduce the phase shift values. Thus, the DTW value is a good measure of the distance between two downsampled autocorrelation signals. We need to compute the DTW values for all downsampled autocorrelation signal pairs, which are then used in stable roommate matching.

**3.4.2 Stable Roommate Matching.** Since the CP decomposed signals are randomly indexed (see Figure 7), we need to identify the pair for each person. With the DTW values for all downsampled autocorrelation signal pairs, we can model this problem as a stable roommate matching problem (Irving 1985; Feng et al. 2015a, 2015b). There is a group of  $2R$  signals, and each signal maintains a preference list of all other signals in the group, where the preference value for another signal is the inverse of the corresponding DTW value (i.e., distance). The problem is to pair the signals such that there is no such pair of signals that both of them have a more desired selection than their current selection (i.e., to find a stable matching) (Irving 1985; Feng et al. 2015a, 2015b). The proposed signal matching algorithm is presented in Algorithm 1.

We first compute the autocorrelation of all decomposed signals. Then, each autocorrelation signal populates its preference list with other autocorrelation signals according to the DTW values. The stable roommate matching algorithm is executed in two steps. In step 1, each signal proposes to other signals according to its preference list. If a signal  $m$  receives a proposal from another signal  $n$ , we implement the following strategy: (i) signal  $m$  rejects signal  $n$  if it has a better proposal from another signal, and (ii) signal  $m$  accepts signal  $n$ 's proposal if it is better than all other proposals that signal  $m$  currently holds. Moreover, signal  $n$  stops to propose when its proposal is accepted and needs to continue to propose to other signals if being rejected. This strategy is implemented in step 1 of the signal matching algorithm, where we use *finish\_flag* to mark whether the current *signal\_num* is accepted or not. Moreover, variables *accept\_num* and *propose\_num* are used to record the current signal's proposed number and proposing number, respectively. In addition, variable *scan\_num* is used to record the current scanning signal number. After completing step 1, every signal holds a proposal or one signal has been rejected by other signals (this case hardly happens in TensorBeat, because the CP decomposition produces two very similar signals with high probability for each person). Then, we need to delete some elements in all preference lists based on the following method, which is that if signal  $m$  is the first on signal  $n$ 's list, then signal  $n$  is the last on signal  $m$ 's list. For the proposed algorithm, every signal can reject signals that have less than *accept\_num* in its preference list symmetrically (reject each other).

An example is shown in Figure 6. According to the DTW values, signals 1, 2, 3, 4, 5, and 6 have their preference lists as (2, 3, 5, 6, 4), (1, 3, 5, 6, 4), (5, 1, 2, 6, 4), (6, 5, 3, 2, 1), (3, 2, 1, 4, 6), and (4, 5, 3, 2, 1), respectively. When step 1 is executed, we have the following: signal 1 proposes to 2, and signal 2 holds 1; signal 2 proposes 1, and signal 1 holds; signal 3 proposes to signal 5, and signal 5 holds; signal 4 proposes to signal 6, and signal 6 holds; signal 5 proposes to signal 3, and signal 3 holds; and signal 6 proposes to signal 4, and signal 4 holds. It is easy to find three pairs (1,2), (3,5), and (4,6).

Although most of decomposed signals are paired in step 1, step 2 will still be necessary for the more challenging cases of many more breathing signals and NLOS environments. In step 2, we consider the reduced preference lists, where some of the lists have more than one signal. By implementing step 2, we can reduce the preference lists such that each signal only holds one proposal. The main idea is that we need to find some all-or-nothing cycles and symmetrically delete signals in the cycle sequence by rejecting the first and last choice pairs. The signal in the

**ALGORITHM 1:** Signal Matching Algorithm**Input:** Decomposed signals:  $S_1, S_2, \dots, S_{2R}$ .**Output:** Matched signal pairs.

Compute autocorrelation of all decomposed signals;

Compute the DTW values for every pair of autocorrelation signals;

Each autocorrelation signal sets its preference list using the DTW values;

//step1;

**for**  $signal\_num = 1 : 2R$  **do**    Set  $finish\_flag = 0$ ;    Set  $scan\_num = signal\_num$ ;    **while**  $finish\_flag = 0$  **do**        **if** *the proposal is the first one* **then**            Proposing signal's  $propose\_num$ =the current choice;            Set  $finish\_flag = 1$ ;            Proposed signal's  $accept\_num = scan\_num$ ;        **else**            **if** *the signal prefers the former proposal* **then**

Reject the current proposal symmetrically;

Propose to the next choice;

**else**

Accept the current proposal;

Reject the former proposal symmetrically;

 $scan\_num =$  proposed signal's  $accept\_num$ ;

Propose to the next choice;

**end**        **end**    **end****end****for**  $signal\_num = 1 : 2R$  **do**    Reject signals that have less than  $accept\_num$  in every preference list symmetrically;**end**

//step2;

 $signal\_num = 1$ ;**while**  $signal\_num < 2R + 1$  **do**    **if**  $propose\_num = accept\_num$  **then**         $signal\_num = signal\_num + 1$ ;    **else**        Let  $p_1$  be a signal whose preference list contains more than one element;        **while**  $p$  sequence is not cyclic **do**             $q_i$  = the second preference of  $p_i$ 's current list;             $p_{i+1}$  = the last preference of  $q_i$ 's current list;        **end**        Denote  $p_s$  as the first element in the  $p$  sequence to be repeated and  $r$  as the length of the circle;        **for**  $i = 1 : r$  **do**            Reject matching  $(q_{s+i-2}, p_{s+i-1})$  symmetrically;        **end**         $signal\_num = 1$ ;    **end****end**

Obtain signal matching pairs based on all processed preference lists;

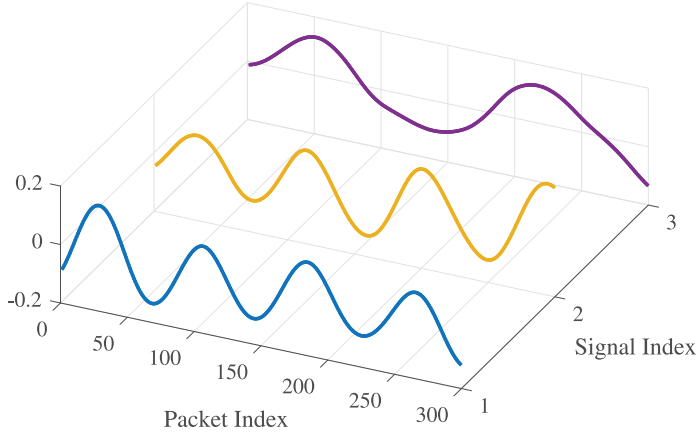


Fig. 9. Fusion results based on the outcomes of the signal matching algorithm.

cycle accepts the secondary choice, thus obtaining a stable roommate matching. To find all-or-nothing cycles, let  $p_1$  be a signal with a preference list that contains more than one element and generate the sequences such that  $q_i$  = the second preference of  $p_i$ 's current list and  $p_{i+1}$  = the last preference of  $q_i$ 's current list. After the cycle sequence generation, denote  $p_s$  as the first element in the  $p$  sequence to be repeated. Then, we reject matching  $(q_s + i - 2, p_s + i - 1)$  for  $i = 1$  to  $r$  symmetrically, where  $r$  is the length of the cycle. Finally, we can obtain signal matching pairs based on all processed preference lists. The computational complexity of Algorithm 1 is  $O(R^2)$ , because each of steps 1 and 2 has a complexity of  $O(R^2)$ , respectively.

### 3.5 Breathing Rate Estimation

**3.5.1 Signal Fusion and Autocorrelation.** After obtaining the outcomes of the signal matching algorithm, TensorBeat next applies peak detection to estimate the breathing rates for multiple persons. Compared to the FFT method, a higher resolution in the time domain can be achieved. To implement peak detection, we first need to combine the decomposed signal pairs for each person into a single signal by taking the average of the signal pairs. Averaging can decrease the variance of the decomposed signals while preserving the same period. For example, Figure 9 shows the fusion results based on the outcome of the signal matching algorithm, where three smoothly decomposed signals with different periods are obtained. To strengthen the accuracy of peak detection, we compute the autocorrelation function again for every fused signal. Figure 10 shows the autocorrelation of the three fused signals. It can be seen that the length of data is increased from 300 to 600 and the number of peaks of every signal are also increased, which help improve estimation accuracy.

**3.5.2 Peak Detection.** Although the breathing signal is generated by the small periodic chest movement of inhaling and exhaling, the phase difference data can effectively capture the breathing rate. Traditionally, estimation of breathing rates is achieved with FFT-based methods. However, the FFT approach may have limited accuracy because the frequency resolution of breathing signals is based on the window size of FFT. When the window size becomes larger, the accuracy will be higher, but the time domain resolution will be reduced. See Figures 2 and 3 for the limitation of the FFT-based approach for the multiperson scenario. Therefore, we leverage peak detection instead in

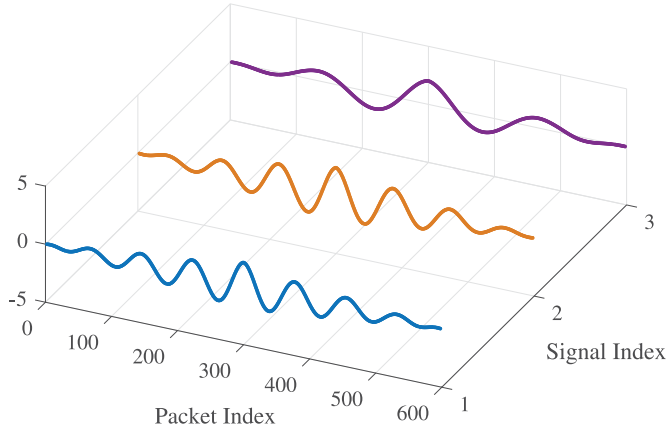


Fig. 10. Autocorrelation of fused signals.

the TensorBeat system to achieve accurate breathing rate estimation for each of autocorrelations of fused signals.

For peak detection, the traditional method based on amplitude needs to detect the fake peak, which is not a real peak but has larger values than its two immediate neighboring points. To avoid the fake peak, a large moving window can be used to identify the real peak based on the maximum breathing periodicity. This method is not robust, since it requires adjusting the window size. In TensorBeat, we only consider a smaller moving window of seven samples wide. This is because we leverage the Hankel matrix and CP decomposition to smooth out the breathing curves, which hardly contain any fake peaks. Then, for the  $i$ th autocorrelation curve of fused signal, we seek all peaks by determining whether or not the median of the seven samples in the moving window is the maximum value. Finally, we consider the median of all peak-to-peak intervals as the final period of the  $i$ th breathing signal, which is denoted as  $T_i$ . The estimated breathing rates can be computed as  $f_i = 60/T_i$  for  $i = 1$  to  $R$ .

## 4 EXPERIMENTAL STUDY

### 4.1 Experiment Configuration

In this section, we validate the TensorBeat performance with an implementation with 5GHz Wi-Fi devices. To obtain 5GHz CSI data, we use a desktop computer and a Dell laptop as access point and mobile device, respectively, both of which are equipped with an Intel 5300 NIC. We use the desktop computer instead of commodity routers, because none is equipped with the Intel 5300 NIC. The operating system is an Ubuntu desktop 14.04 LTS OS for both the access point and the mobile device. The PHY is the IEEE 802.11n OFDM system with QPSK modulation and 1/2 coding rate. Moreover, the access point is set in the monitor model, and the distance between its two adjacent antennas is approximately 2.68cm, which is half of the wavelength of 5GHz WiFi. In addition, the mobile device is set in the injection model and uses one antenna to transmit data. Moreover, we use omnidirectional antennas for both the receiver and transmitter to estimate breathing signs beats. With the packet injection technique with LORCON version 1, we can obtain 5GHz CSI data from the three antennas of the receiver.

Our experimental study is with up to five persons over a period of 6 months. The experimental scenarios include a computer laboratory, a through-wall scenario, and a corridor, as shown in Figure 11. The first scenario is within a  $4.5 \times 8.8 \text{ m}^2$  laboratory, where both single-person and

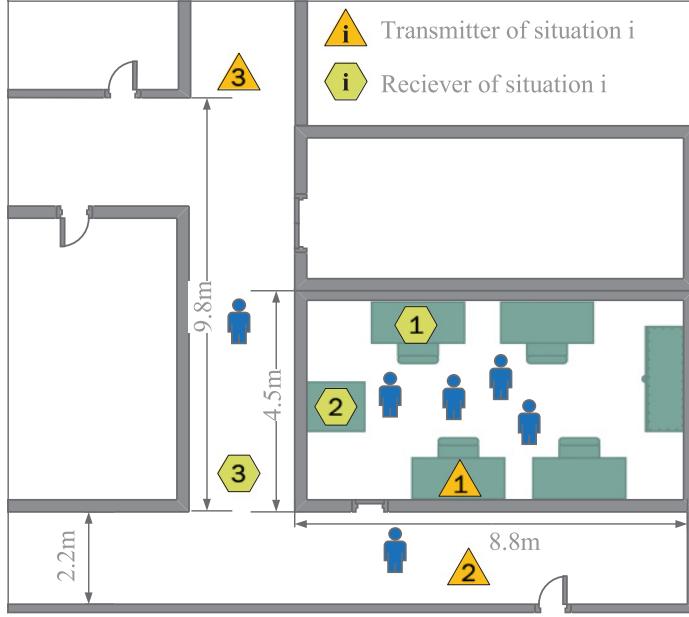


Fig. 11. Experimental setup: computer laboratory, through-wall, and long corridor scenarios.

multiperson breathing rate estimation experiments are conducted. There are lots of tables and desktop computers crowded in the laboratory, which block parts of the LOS paths and form a complexity radio propagation environment. The second setup is a through-wall environment, where single-person breathing rate estimation is tested due to the relatively weaker signal reception. The person is on the transmitter side, and the receiver is behind a wall in this experiment. The third scenario is a long corridor of 20m, where the maximum distance between the receiver and transmitter is 11m in the experiment. These scenarios are also considered for single-person breathing rate monitoring. We use NEULOG Respiration to record the ground truths for single-person breathing rates. Single-person breathing rate estimation can be easily implemented by removing the signal matching algorithm, because there are only two decomposed signals after CP decomposition in this case. For multiperson breathing rate estimation in the first scenario, all persons participating in the experiment record their breathing rates by using a metronome smartphone application with 1 beat per minute (bpm) accuracy at the same time. We consider that five persons are stationary for LOS and NLOS environments for breathing monitoring. Moreover, there are no other persons in the breathing measurement area.

For multiperson breathing rate estimation, we need to define a proper metric for evaluating TensorBeat's performance. For  $R$  estimated breathing rates  $[f_1, f_2, \dots, f_R]$ , the  $i$ th breathing rate estimation error,  $E_i$ , is defined as

$$E_i = |f_i - \hat{f}_i| \text{ for } i = 1, 2, \dots, R, \quad (34)$$

where  $\hat{f}_i$  is the ground truth of the  $i$ th breathing rate. We also define a new metric termed success rate, denoted as  $SR$ , which is defined as

$$SR = \frac{N\{\max_i \{E_i\} < 2\text{bpm}\}}{N\{E\}} \times 100\%, \quad (35)$$



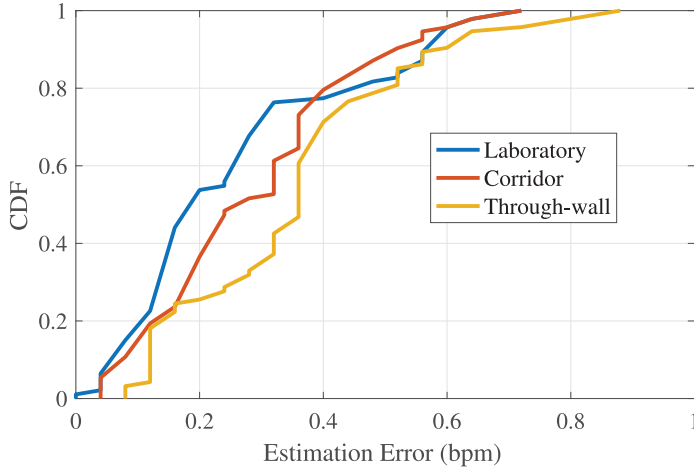


Fig. 12. Performance of single-person breathing rate estimation in the computer laboratory, through-wall, and long corridor scenarios.

where  $N\{\max_i \{E_i\} < 2\text{bpm}\}$  means the number of repeated experiments of the maximum breathing rate error less than 2 bpm and  $N\{E\}$  is the number of repeated experiments. We adopt the success rate metric because there are weak signals for multiperson experiments in indoor experiments at different locations, and sometimes a breathing signal may not be successfully detected (Wang et al. 2016a, 2017b).

#### 4.2 Performance of Breathing Rate Estimation

In Figure 12, we present the cumulative distribution functions (CDFs) of the estimation errors for single-person breathing rate detection for three different experiment scenarios. We can see that for TensorBeat, high estimation accuracy of breathing rates can be achieved in all three scenarios. The maximum estimation error is less than 0.9 bpm. Moreover, it is noticed that 50% of the tests for the computer laboratory experiment have errors less than about 0.19 bpm, whereas the tests for the corridor and through-wall scenarios have errors less than approximately 0.25 bpm and 0.35 bpm, respectively. Thus, the performance in the laboratory setting is better than that in the corridor and through-wall scenarios. This is because the laboratory has a smaller space and the breathing signal is stronger than that of other two cases with larger attenuation due to the long distance and the wall.

Figure 13 presents the performance of breathing rate estimation for different numbers of persons. It is noticed that higher accuracy is achieved for the single-person test, where approximately 96% of the test data have an estimation error less than 0.5 bpm. The five-person test has the worse performance, where approximately 62% of the test data has an estimation error less than 0.5 bpm. Moreover, we find that the performance of the two- and three-person tests are similar, both of which have an error smaller than 0.5 bpm for 93% of the test data. Generally, when the number of persons is increased, the performance of breathing rate estimation becomes worse. In fact, when the number of breathing signals is increased, the distortion of the mixed received signal will become larger, thus leading to high estimation errors.

Figure 14 plots the success rates for different numbers of persons. We find that although the success rate for one person is the highest, there are still a few of the test data that cannot obtain high-accuracy breathing rate estimation. These test data should come from different locations in

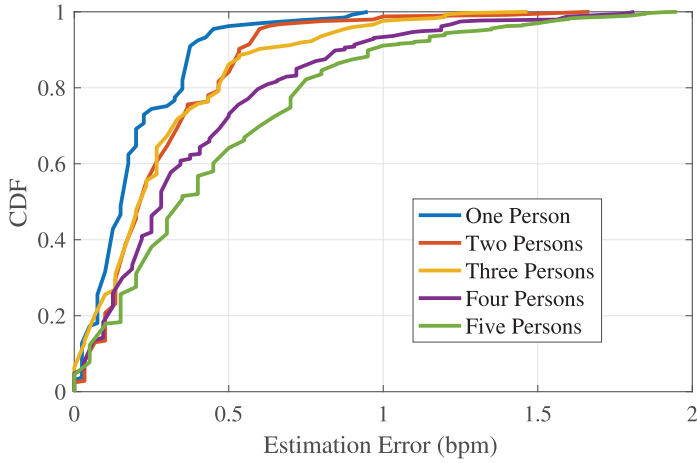


Fig. 13. Performance of breathing rate estimation for different numbers of persons (computer laboratory).

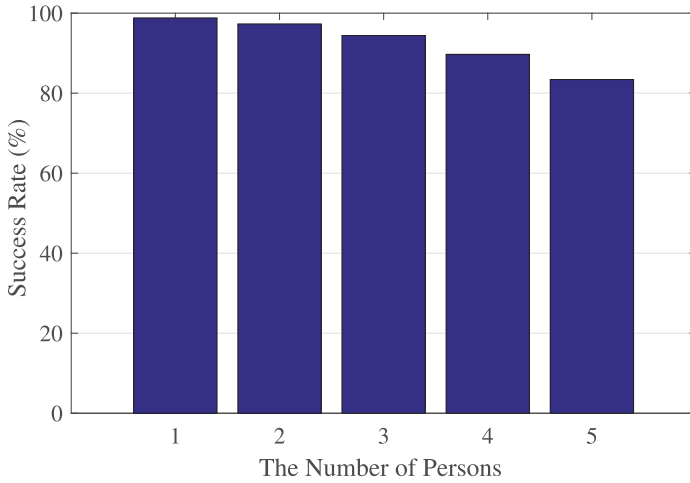


Fig. 14. Success rates for different numbers of persons (computer laboratory).

the indoor environments, where parts of the received signals are severely distorted. In fact, we find that low phase difference usually occurs when the SNR is low. However, we can see that breathing rate estimation for two persons also has a high success rate, because the probability for two persons to have exactly the same breathing rate is very low. When the number of persons is increased, the chance of getting two close breathing rates becomes higher. Even in this case, TensorBeat can still effectively separate them with a high success probability. With the increase in the number of persons, the success rate for the TensorBeat system decreases. The reason is that each breathing rate is more likely to cover each other and the strength of the received signal becomes lower. From Figure 14, we can see that the success rate is about 82.4% when the number of persons is five.

Figure 15 shows the success rate for different sampling rates. In this experiment, there are four persons and the window size is set to 30s. From Figure 15, we can see that with the increase in the number of sampling rates, the success rate is also increased. It is noticed that the success rates

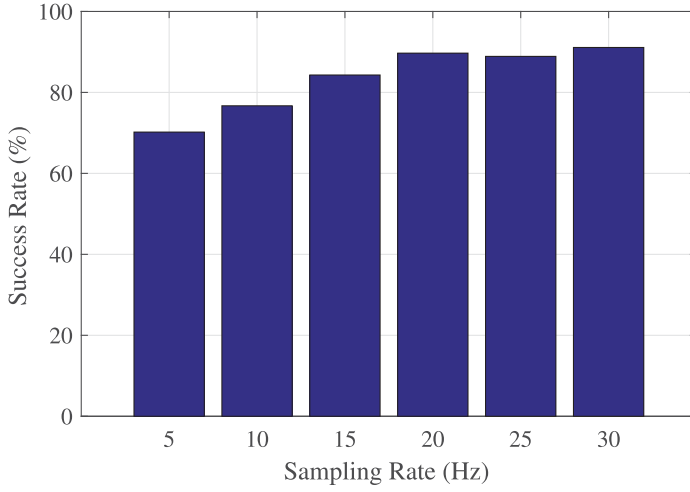


Fig. 15. Success rates for different sampling rates (computer laboratory).

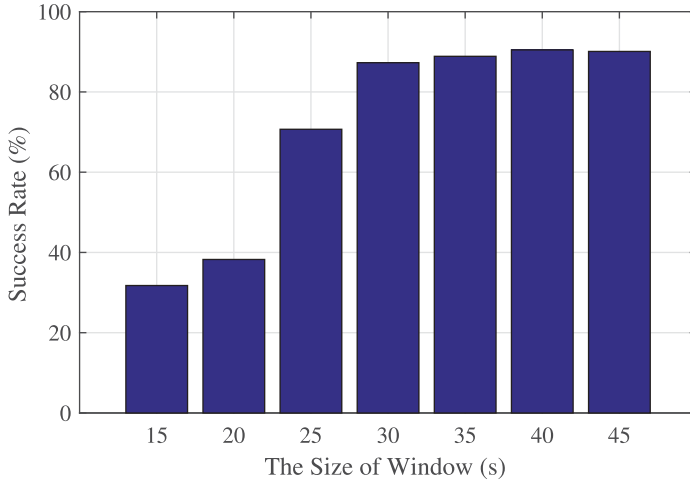


Fig. 16. Success rates for different window sizes (computer laboratory).

for 5Hz and 30Hz are approximately 70% and 90%, respectively. As the sampling rate is increased, the length of the data for CP decomposition is increased for the 30s window size case, which helps to improve estimation accuracy. Furthermore, we find that the performance becomes stable when the sampling rate exceeds 20Hz, indicating that a sampling rate of 20Hz is sufficient for CP decomposition. Thus, we set the sampling rate to 20Hz for the TensorBeat experiments.

Figure 16 plots the success rates for different window sizes. This experiment is for the computer laboratory scenario with four persons and a sampling rate set to 20Hz. From this figure, we can see that the success rate is greatly increased by increasing the window size of the Hankel matrix from 15 to 30 s. This is because Hankelization will take half of the data to smooth the phase difference signal, which reduces the resolution in the time domain. Thus, we need to increase the window size to improve estimation accuracy. Furthermore, the change of success rate is small for window sizes from 30 to 45 s. Thus, we select a window size of 30 s for the TensorBeat experiments.

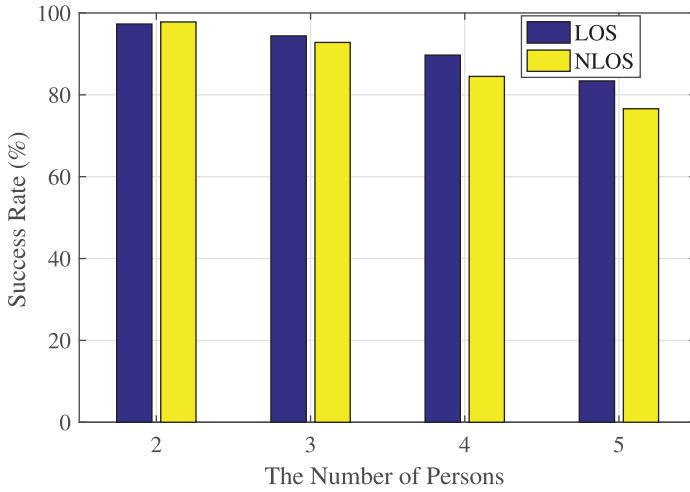


Fig. 17. Success rates for when multiple persons form a line in the LOS path between the transmitter and receiver, and when multiple persons are scattered around (computer laboratory).

Finally we examine the impact of LOS and NLOS scenarios. The success rates are plotted in Figure 17. In this experiment, we consider the challenge condition of the NLOS scenario, where all persons stay on the LOS path between the transmitter and receiver—that is, they form a straight line and block each other. From Figure 15, we find that the performance for LOS and NLOS are nearly the same for the cases of two or three persons, where high estimation accuracy can be achieved. This is due to the WiFi multipath effect, which is regarded harmful in general but becomes helpful in breathing rate estimation when tensor decomposition is used. The breathing signal of every person can still be captured at the receiver from the phase difference data. However, when the number of persons is further increased, the success rate decreases quickly. In fact, the strength of the breathing signals for some persons becomes too weak to be detected when there are too many people blocking each other.

## 5 RELATED WORK

This work is closely related to sensor- and RF signal-based vital signs monitoring, as well as CSI-based indoor localization and human activity recognition, which are discussed in the following.

Sensor-based vital signs monitoring with wearable and smart devices employs special hardware attached to a person's body to monitor breathing and heart rate data. The capnometer can measure carbon dioxide ( $\text{CO}_2$ ) concentrations in respired gases, which are employed to monitor a patient's breathing rate in the hospital. However, it is uncomfortable for patients to wear them, which are thus leveraged in clinical environments (Mogue and Rantala 1988). Photoplethysmography (PPG) is an optical technique to monitor blood volume changes in tissues by measuring light absorption changes, thus requiring sensors attached to a person's finger, such as the pulse oximeter (Shariati and Zahedi 2005). In addition, a smartphone can use the camera to detect light changes from the video frames that can extract the PPG signal to monitor the heart rate (Scully et al. 2010). Moreover, smartphones can also estimate the breathing rate by using the built-in accelerometer, gyroscope (Aly and Youssef 2016), and microphone (Ren et al. 2015), which require persons to have smartphones nearby and wear sensors for breathing monitoring. However, techniques based on sensors cannot be applied for remote monitoring of vital signs.

RF-based systems for vital sign monitoring use wireless signals to track breathing-induced chest changes in a person, which are mainly based on radar and WiFi techniques. For radar-based vital signals monitoring, Vital-Radio employs FMCW radar to estimate breathing and heart rates, even for two subjects in parallel (Adib et al. 2015). But the system requires a customized hardware with a large bandwidth from 5.46 to 7.25 GHz. For WiFi-based vital signs monitoring, the UbiBreathe system employs WiFi RSS for breathing rate monitoring, which, however, requires the device placed in the LOS path between the transmitter and the receiver for estimating the breathing rate (Abdelnasser et al. 2015). Moreover mmVital based on RSS can use 60 GHz millimeter wave (mmWave) signal for breathing and heart rates monitoring with large bandwidth about 7GHz, which does not work well over a longer distance and require high gain directional antennas for the transmitter and the receiver (Yang et al. 2016; Gong et al. 2010). Recently, the authors have leveraged the amplitudes of CSI data to monitoring vital signs (Liu et al. 2015). This work is mainly to track vital signs when a person is sleeping, which is limited for monitoring a maximum of two persons at the same time.

In addition to vital signs monitoring, CSI-based sensing systems recently have also been used for indoor localization and human activity recognition (Cushman et al. 2016). CSI-based fingerprinting systems have been proposed to obtain high localization accuracy. FIFS is the first work to use the weighted average of CSI amplitude values over multiple antennas for indoor localization (Xiao et al. 2012). To exploit the diversity among the multiple antennas and subcarriers, DeepFi leverages 90 CSI amplitude data from the three antennas with a deep autoencoder network for indoor localization (Wang et al. 2015c, 2017a). In addition, PhaseFi leverages calibrated CSI phase data for indoor localization based on deep learning (Wang et al. 2015b, 2016b). Different from CSI-based fingerprinting techniques, the SpotFi system leverages a superresolution algorithm to estimate the angle of arrival of multipath components for indoor localization based on CSI data from three antennas (Kotaru et al. 2015). The E-eyes system leverages CSI amplitude values for recognizing household activities such as washing dishes and taking a shower (Wang et al. 2014c). The WiHear system employs specialized directional antennas to measure CSI changes from lip movement for determining spoken words (Wang et al. 2014a). The CARM system considers a CSI-based speed model and a CSI-based activity model to build the correlation between CSI data dynamics and a given human activity (Wang et al. 2015a). Although CSI-based sensing is effective for indoor localization and activity recognition, there are few works for using CSI phase difference data to detect multiperson behavior at the same time.

The TensorBeat system is motivated by these interesting prior works. To the best of our knowledge, we are the first to leverage CSI phase difference data for multiperson breathing rate estimation. We are also the first to employ tensor decomposition for RF sensing-based vital sign monitoring, which can also be employed for indoor localization and human activity recognition.

## 6 CONCLUSIONS

In this article, we proposed TensorBeat—tensor decomposition for estimating multiperson breathing beats with commodity WiFi. The proposed TensorBeat system employed CSI phase difference data to obtain the periodic signals from the movements of multiple breathing chests by leveraging tensor decomposition. We implemented several signal processing methods, including data preprocessing, CP decomposition, the signal matching algorithm, and peak detection, in TensorBeat. We validated the performance of TensorBeat with extensive experiments under three indoor environments. Our analysis and experimental study demonstrated that the proposed TensorBeat system can achieve satisfactory performance for multiperson breathing estimation.

## REFERENCES

- H. Abdelnasser, K. A. Harras, and M. Youssef. 2015. Ubibreathe: A ubiquitous non-invasive WiFi-based breathing estimator. In *Proceedings of the IEEE MobiHoc Conference (MobiHoc'15)*. ACM, New York, NY, 277–286.
- F. Adib, H. Mao, Z. Kabelac, D. Katabi, and R. Miller. 2015. Smart homes that monitor breathing and heart rate. In *Proceedings of the ACM CHI Conference (CHI'15)*. ACM, New York, NY, 837–846.
- H. Aly and M. Youssef. 2016. Zephyr: Ubiquitous accurate multi-sensor fusion-based respiratory rate estimation using smartphones. In *Proceedings of the IEEE INFOCOM Conference (INFOCOM'16)*. IEEE, Los Alamitos, CA, 1–9.
- O. Boric-Lubeke and V. M. Lubecke. 2002. Wireless house calls: Using communications technology for health care and monitoring. *IEEE Microwave Magazine* 3, 3, 43–48.
- A. Cichocki, D. P. Mandic, L. De Lathauwer, G. Zhou, Q. Zhao, C. F. Caiafa, and A. H. Phan. 2015. Tensor decompositions for signal processing applications: From two-way to multiway component analysis. *IEEE Signal Processing Magazine* 32, 2, 145–163.
- I. Cushman, D. B. Rawat, A. Bhimraj, and M. Fraser. 2016. Experimental approach for seeing through walls using Wi-Fi enabled software defined radio technology. *Digital Communications and Networks* 2, 4, 245–255.
- A. Droitcour, O. Boric-Lubecke, and G. Kovacs. 2009. Signal-to-noise ratio in Doppler radar system for heart and respiratory rate measurements. *IEEE Transactions on Microwave Theory and Techniques* 57, 10, 2498–2507.
- M. Feng, S. Mao, and T. Jiang. 2015a. Duplex mode selection and channel allocation for full-duplex cognitive femtocell networks. In *Proceedings of the IEEE WCNC Conference (WCNC'15)*. IEEE, Los Alamitos, CA, 1900–1905.
- M. Feng, S. Mao, and T. Jiang. 2015b. Joint duplex mode selection, channel allocation, and power control for full-duplex cognitive femtocell networks. *Digital Communications and Networks* 1, 1, 30–44.
- J. Gjengset, J. Xiong, G. McPhillips, and K. Jamieson. 2014. Phaser: Enabling phased array signal processing on commodity WiFi access points. In *Proceedings of the ACM MobiCom Conference (MobiCom'14)*. ACM, New York, NY, 153–164.
- M. X. Gong, R. J. Stacey, D. Akhmetov, and S. Mao. 2010. A directional CSMA/CA protocol for mmWave wireless PANs. In *Proceedings of the IEEE WCNC Conference (WCNC'10)*. IEEE, Los Alamitos, CA, 1–6.
- D. Halperin, W. J. Hu, A. Sheth, and D. Wetherall. 2010. Predictable 802.11 packet delivery from wireless channel measurements. In *Proceedings of the ACM SIGCOMM Conference (SIGCOMM'10)*. ACM, New York, NY, 159–170.
- H. Hu, Y. G. Wen, T.-S. Chua, and X. L. Li. 2014. Towards scalable systems for big data analytics: A technology tutorial. *IEEE Access Journal* 2, 652–687.
- C. Hunt and F. Hauck. 2006. Sudden infant death syndrome. *Canadian Medical Association Journal* 174, 13, 1309–1310.
- R. Irving. 1985. An efficient algorithm for the ‘stable roommates’ problem. *Journal of Algorithms* 6, 6, 577–595.
- T. G. Kolda and B. W. Bader. 2009. Tensor decompositions and applications. *SIAM Review* 51, 3, 455–500.
- M. Kotaru, K. Joshi, D. Bharadia, and S. Katti. 2015. SpotFi: Decimeter level localization using WiFi. In *Proceedings of the ACM SIGCOMM Conference (SIGCOMM'15)*. ACM, New York, NY, 269–282.
- L. De Lathauwer. 2011. Blind separation of exponential polynomials and the decomposition of a tensor in rank-( $L_r$ ,  $L_r$ , 1) terms. *SIAM Journal on Matrix Analysis and Applications* 32, 4, 1451–1474.
- Y. LeCun, Y. Bengio, and G. Hinton. 2015. Deep learning. *Nature* 521, 7553, 436–444.
- J. Liu, Y. Wang, Y. Chen, J. Yang, X. Chen, and J. Cheng. 2015. Tracking vital signs during sleep leveraging off-the-shelf WiFi. In *Proceedings of the ACM MobiHoc Conference (MobiHoc'15)*. ACM, New York, NY, 267–276.
- Y. Luo, D. C. Tao, Y. G. Wen, R. Kotagiri, and C. Xu. 2015. Tensor canonical correlation analysis for multi-view dimension reduction. *IEEE Transactions on Knowledge and Data Engineering* 27, 11, 3111–3124.
- M. L. R. Mogue and B. Rantala. 1988. Capnometers. *Journal of Clinical Monitoring* 4, 115–121.
- E. E. Papalexakis, C. Faloutsos, and N. D. Sidiropoulos. 2016. Tensors for data mining and data fusion: Models, applications, and scalable algorithms. *ACM Transactions on Intelligent Systems and Technology* 8, 2, 16:1–16:44.
- Kun Qian, Chenshu Wu, Zheng Yang, Yunhao Liu, and Zimu Zhou. 2014. PADS: Passive detection of moving targets with dynamic speed using PHY layer information. In *Proceedings of the IEEE ICPADS Conference (ICPADS'14)*. IEEE, New York, NY, 1–8.
- P. Rashidi and D. J. Cook. 2013. COM: A method for mining and monitoring human activity patterns in home-based health monitoring systems. *ACM Transactions on Intelligent Systems and Technology* 4, 4, 64:1–64:20.
- Y. Ren, C. Wang, J. Yang, and Y. Chen. 2015. Fine-grained sleep monitoring: Hearing your breathing with smartphones. In *Proceedings of the IEEE INFOCOM Conference (INFOCOM'15)*. IEEE, Los Alamitos, CA, 1194–1202.
- J. Salmi and A. F. Molisch. 2011. Propagation parameter estimation, modeling and measurements for ultrawideband MIMO radar. *IEEE Transactions on Microwave Theory and Techniques* 59, 11, 4257–4267.
- S. Salvador and P. Chan. 2004. FastDTW: Toward accurate dynamic time warping in linear time and space. In *Proceedings of the KDD Workshop on Mining Temporal Sequential Data*. ACM, New York, NY, 70–80.
- S. Salvador and P. Chan. 2007. Toward accurate dynamic time warping in linear time and space. *Intelligent Data Analysis Journal* 11, 5, 561–580.



- C. G. Scully, J. Lee, J. Meyer, A. M. Gorbach, D. Granquist-Fraser, Y. Mendelson, and K. H. Chon. 2010. Physiological parameter monitoring from optical recordings with a mobile phone. *IEEE Transactions on Biomedical Engineering* 59, 2, 303–306.
- N. H. Shariati and E. Zahedi. 2005. Comparison of selected parametric models for analysis of the photoplethysmographic signal. In *Proceedings of the CCSP Conference (CCSP'05)*. IEEE, Los Alamitos, CA, 169–172.
- M. Speth, S. Fechtel, G. Fock, and H. Meyr. 1999. Optimum receiver design for wireless broad-band systems using OFDM—Part I. *IEEE Transactions on Communications* 47, 11, 1668–1677.
- Y. Sun and M. Kumar. 2014. Numerical solution of high dimensional stationary Fokker-Planck equations via tensor decomposition and Chebyshev spectral differentiation. *Computers and Mathematics with Applications* 67, 10, 1960–1977.
- Y. Sun and M. Kumar. 2015. A numerical solver for high dimensional transient Fokker-Planck equation in modeling polymeric fluids. *Journal of Computational Physics* 289, 10, 149–168.
- D. P. Tao, Y. G. Wen, and R. C. Hong. 2016. Multi-column bi-directional long short-term memory for mobile devices-based human activity recognition. *IEEE Internet of Things Journal* 3, 6, 1124–1134.
- G. Wang, Y. Zou, Z. Zhou, K. Wu, and L. Ni. 2014a. We can hear you with Wi-Fi! In *Proceedings of the ACM MobiCom Conference (MobiCom'14)*. ACM, New York, NY, 593–604.
- H. Wang, D. Zhang, J. Ma, Y. Wang, Y. Wang, D. Wu, T. Gu, and B. Xie. 2016a. Human respiration detection with commodity WiFi devices: Do user location and body orientation matter? In *Proceedings of the UbiComp Conference (UbiComp'16)*. ACM, Los Alamitos, CA, 25–36.
- J. Wang and D. Katabi. 2013. Dude, where's my card? RFID positioning that works with multipath and non-line of sight. In *Proceedings of the ACM SIGCOMM Conference (SIGCOMM'13)*. ACM, New York, NY, 51–62.
- W. Wang, A. Liu, M. Shahzad, K. Ling, and S. Lu. 2015a. Understanding and modeling of WiFi signal based human activity recognition. In *Proceedings of the ACM MobiCom Conference (MobiCom'15)*. ACM, New York, NY, 65–76.
- X. Wang, L. Gao, and S. Mao. 2015b. PhaseFi: Phase fingerprinting for indoor localization with a deep learning approach. In *Proceedings of the GLOBECOM Conference (GLOBECOM'15)*. IEEE, Los Alamitos, CA, 1–6.
- X. Wang, L. Gao, and S. Mao. 2016b. CSI phase fingerprinting for indoor localization with a deep learning approach. *IEEE Internet of Things Journal* 3, 6, 1113–1123.
- X. Wang, L. Gao, S. Mao, and S. Pandey. 2015c. DeepFi: Deep learning for indoor fingerprinting using channel state information. In *Proceedings of the WCNC Conference (WCNC'15)*. IEEE, Los Alamitos, CA, 1666–1671.
- X. Wang, L. Gao, S. Mao, and S. Pandey. 2017a. CSI-based fingerprinting for indoor localization: A deep learning approach. *IEEE Transactions on Vehicular Technology* 66, 1, 763–776.
- X. Wang, C. Yang, and S. Mao. 2017b. PhaseBeat: Exploiting CSI phase data for vital sign monitoring with commodity WiFi devices. In *Proceedings of the IEEE ICDCS Conference (ICDCS'17)*. IEEE, Atlanta, GA, 1230–1239.
- X. Wang, S. Mao, and M. X. Gong. 2016c. A survey of LTE Wi-Fi coexistence in unlicensed bands. *ACM GetMobile: Mobile Computing and Communications* 20, 3, 17–23.
- X. Wang, S. Mao, S. Pandey, and P. Agrawal. 2014b. CA2T: Cooperative antenna arrays technique for pinpoint indoor localization. In *Proceedings of the MobiSPC Conference (MobiSPC'14)*. 392–399.
- Y. Wang, J. Liu, Y. Chen, M. Gruteser, J. Yang, and H. Liu. 2014c. E-eyes: Device-free location-oriented activity identification using fine-grained WiFi signatures. In *Proceedings of the ACM MobiCom Conference (MobiCom'14)*. ACM, New York, NY, 617–628.
- Chenshu Wu, Zheng Yang, Zimu Zhou, Kun Qian, Yunhao Liu, and Mingyan Liu. 2015. PhaseU: Real-time LOS identification with WiFi. In *Proceedings of the IEEE INFOCOM Conference (INFOCOM'15)*. IEEE, Los Alamitos, CA, 2038–2046.
- Z. L. Wu, C. H. Li, J. K. Y. Ng, and K. R. P. H. Leung. 2007. Location estimation via support vector regression. *IEEE Transactions on Mobile Computing* 6, 3, 311–321.
- J. Xiao, K. Wu, Y. Yi, and L. M. Ni. 2012. FIFS: Fine-grained indoor fingerprinting system. In *Proceedings of the IEEE ICCCN Conference (ICCCN'12)*. ACM, New York, NY, 1–7.
- Y. Xie, Z. Li, and M. Li. 2015. Precise power delay profiling with commodity WiFi. In *Proceedings of the ACM MobiCom Conference (MobiCom'15)*. ACM, New York, NY, 53–64.
- Y. Xu, G. Yue, and S. Mao. 2014. User grouping for massive MIMO in FDD systems: New design methods and analysis. *IEEE Access Journal* 2, 1, 947–959. <http://dx.doi.org/10.1109/ACCESS.2014.2353297>
- Z. Yang, P. Pathak, Y. Zeng, X. Liran, and P. Mohapatra. 2016. Monitoring vital signs using millimeter wave. In *Proceedings of the IEEE MobiHoc Conference (MobiHoc'16)*. ACM, New York, NY, 211–220.
- Z. Yang, Z. Zhou, and Y. Liu. 2013. From RSSI to CSI: Indoor localization via channel response. *ACM Computing Surveys* 46, 2, 25:1–25:32.

Received November 2016; revised January 2017; accepted February 2017